AgriEngineering

MDPI

Article

Can Hyperspectral Reflectance Thresholds Achieve Spatial Partitioning of Sweet Potato Leaf Deformation Types on UAV Multispectral Imagery?

Sinesipho Fose [1], Adolph Nyamugama [2] and Naledzani Ndou [3,*]

[1] Department of Chemical and Earth Sciences, University of Fort Hare, 50 Church Street, East London 5201, South Africa
[2] Agricultural Research Council, Natural Resource and Engineering (ARC-NRE), Pretoria 0001, South Africa
[3] Department of Geography, University of South Africa (UNISA), Florida, Roodepoort 1709, South Africa
* Correspondence: ndounn@unisa.ac.za

Abstract

Timely detection and monitoring of diseases in sweet potato crops are important for hunger alleviation and food security. This study aimed to evaluate the efficacy of the optimized field spectrometric reflectance thresholds in spatially partitioning sweet potato crops on the unmanned aerial vehicle (UAV) multispectral imagery based on infection types. A field survey was carried out to sample deformed leaves for laboratory diagnosis of possible identification of sweet potato leaf infection types. Laboratory analysis results revealed nutrient deficiency, SPVC-positive, fungi isolates (i.e., *alternaria*, *bipolaris*, *fusarium*, *phoma*), and mechanical damage as the causes of leaf deformation. Overlap analysis results revealed reflectance overlaps across all leaf deformation types, making it difficult to spatially partition sweet potato crops based on deformation types. Instead, sweet potato crops were spatially partitioned by considering the minimum and maximum thresholds acquired from the whole dataset. Area covered by deformed sweet potato leaves in blue, green, red, red edge and NIR were found to be 11.91%, 28.71%, 43.66%, 46.41% and 30.6% respectively. Coefficient of determination results revealed poor classification results, with R^2 value of 0.23, 0.19, 0.28, 0.17 and 0.63 for blue, green, red, red edge and NIR respectively. However, the NIR spectral band yielded R^2 value closer to the acceptable value of 0.7.

Keywords: sweet potato; deformed leaves; hyperspectral reflectance; unmanned aerial vehicle; thresholding

Check for updates

Academic Editor: Ray E. Sheriff

Received: 5 October 2025
Revised: 28 May 2026
Accepted: 6 June 2026
Published: 23 June 2026

Copyright: © 2026 by the authors. Licensee MDPI, Basel, Switzerland. This article is an open access article distributed under the terms and conditions of the Creative Commons Attribution (CC BY) license.

1. Introduction

Sweet potato, just like any other crop, is susceptible to diseases, which tend to hinder its productivity and yield. Sweet potato diseases are prevalent in small-scale farms, which are characterized by a lack of financial resources to minimize or avoid the impact of these diseases. These diseases often manifest on sweet potato leaves, making sweet potato leaves a suitable crop parameter for monitoring infected sweet potato. An infected sweet potato leaf may exhibit mild circular spots or light-green patterns along its veins, subsequently causing leaf deformation, mosaic symptoms, yellowing, vein clearing, dwarfing, stunting, and wilting [1]. These diseases tend to be exacerbated when climate patterns shift to foster favorable conditions for these diseases [2]. Thompson and Domola [3] identified four most common diseases that are prevalent on sweet potato leaves, and these are the sweet potato

feathery mottle virus (SPFMV), sweet potato mild mottle virus (SPMMV), sweet potato chlorotic stunt virus (SPCSV), sweet potato virus C (SPVC) and sweet potato virus disease (SPVD). The leaves infected with these diseases often experience reduction in chlorophyll content and subsequently photosynthetically active radiation [4]. Therefore, accurate characterization and spatial partitioning of infected sweet potato leaves are important for understanding distribution and for informed decision making regarding appropriate intervention strategy for improving yield [5].

Conventionally, detection of infected sweet potato leaves is usually based on the detection of leaf deformation using the on-site visual observation. However, this approach is subjective, laborious, time-consuming, costly [6], limited to detection of leaf deformation and cannot differentiate various types of leaf infections. As such, this approach is often accompanied by sampling of deformed leaves for laboratory diagnosis of infections. Moreover, this approach is only effective when a leaf exhibits clearly visible symptoms, which usually manifest at the middle to late stage of infection [7]. This is because disease often starts on a single leaf, making it impossible to detect through visual inspection at an early stage. As such, implementation of early intervention process to manage the infection before it spreads throughout the entire field becomes impossible [7]. However, visual observation and laboratory diagnosis approaches can be integrated with modern technologies to enhance detection of leaf deformation for infection diagnosis. Remote sensing technology has demonstrated the ability to overcome the limitations associated with the visual observation approach in detecting leaf detection. Deformed leaves may exhibit spectral reflectance properties that are different from healthy leaves, making it possible to spectrally characterize them [8–10]. When crop leaf is infected, its internal structure, leaf water content and pigment contents change, making remote sensing a viable tool to analyze their spectral reflectance deviation from healthy leaves [11,12]. Moreover, remote sensing techniques are deployed in the detection of infected crops [13], without causing damage to crops.

Satellite sensors such as Landsat generations [14,15] and Sentinel-2 multispectral imager [16] have been used to detect infected crops, taking advantage of their visible-near-infrared (VIS-NIR) and shortwave infrared (SWIR) spectral wavelengths sensitive to changes in leaf deformation. Nonetheless, these multispectral sensors have shown limitations to distinctly identify infected crops in small-scale farm plots whose sizes are characteristically smaller than spatial resolutions of these sensors. Unmanned aerial vehicle (UAV) multispectral imaging systems have demonstrated their efficacy in mapping crops over small-scale plots due to their ultra-high spatial resolution [17]. These systems can offer detailed information about crop health at a spatial resolution of a few centimeters [18]. Several studies have deployed these imaging systems to characterize infected crops [19,20]. However, these systems are also not without limitations; despite their ultra-high spatial resolution, the end products of these systems are highly susceptible to noise because of their ability to detect very small, trivial land features that subsequently cause spectral confusion. Non-imaging hyperspectral system offers ultra-high spectral resolution data, making it suitable for identifying specific infected crops based on detailed spectral signatures [21]. Using this system, even a slight deviation in the reflectance properties of an infected leaf can be detected [22]. This is because non-imaging systems acquire spectral information about crops at leaf scale, in contrast to UAV systems that attain crop information at canopy scale. In this study, it is envisaged that using crop spectral data acquired at leaf scale to spatially partition UAV image can offer an effective way for spatially characterizing infected sweet potato leaves.

Spatial partitioning of crop characterization on canopy scale can be achieved by thresholding of UAV imagery based on non-imaging hyperspectral data acquired on a leaf

scale [23]. Despite its status as an ancient image classification method and recent advances in pattern cognizance through machine/deep learning approaches [19,24], recent studies continue to recommend thresholding (rule-based classifiers) for spatial partitioning of image [25–27]. In particular, a multilevel thresholding (MLT) classifier was established to segment the image into multiple categories. This approach also proved to be able to partition complex features in an image [27], just like spectrally overlapping features. The relevance of this approach in the current study was to overcome limitations associated with conventional classification approaches that rely on empirical or arbitrarily defined thresholds, as this study attempts to spatially partition infected sweet potato crops by utilizing spectral reflectance thresholds obtained directly from descriptive statistics of laboratory-confirmed deformed leaf samples. However, optimization of thresholding is required if accurate image partitioning is to be achieved. Several approaches have been devised to improve thresholds and minimize uncertainties in established classes. These approaches include interquartile range [28], k-sigma [29], percentile [30], maximum [31] and Kernel density estimation [32]. Among these methods, the k-sigma approach displayed simplicity; it relies on the mean and standard deviation computed from datasets assumed to be normally distributed [33].

In their study to detect infected maize crops, Nkuna et al. [2] used the spectral indices derived from spectral signatures acquired from the non-imaging hyperspectral sensing system. Feng et al. [8] used hyperspectral non-imaging system to monitor mildew disease severity in wheat. Lowe et al. [7] also detected and classified the early onset of plant disease based on hyperspectral analysis techniques. Based on a literature search, we noted that studies that use non-imaging hyperspectral reflectance data to spatially partition infected crops are lacking. The novelty of this study lies in the integration of non-imaging hyperspectral ASD data with UAV multispectral imagery to derive physically informed thresholds for the spatial classification of infected sweet potato crops. These thresholds are subsequently transferred to UAV-derived spectral bands to enable the spatial configuration of infection patterns. This approach is one of a kind since it links field-based spectral measurements with aerial imagery for improved disease detection in smallholder crop farming systems.

2. Materials and Methods

2.1. Study Area

This study was conducted in the Dzimauli small-scale area, situated in the Mutale River catchment in the Vhembe District of Limpopo Province of South Africa. The small-scale farm surveyed in the study area was located within 22°47′46.787″ S, 30°28′26.211″ E and 22°47′54.926″ S, 30°28′32.752″ E grid references. Crop farming is one of the major activities practiced in the study area. The crops cultivated in the study area include sweet potato, maize, green beans, Florida broadleaf mustard, and sugar beans [34]. The selection of the study area was prompted by the inability of farmers to identify disease types through visual inspection which may subsequently limit them to devise appropriate remedial paths to restoring crop health state. Figure 1 represents the location settings of the study area.

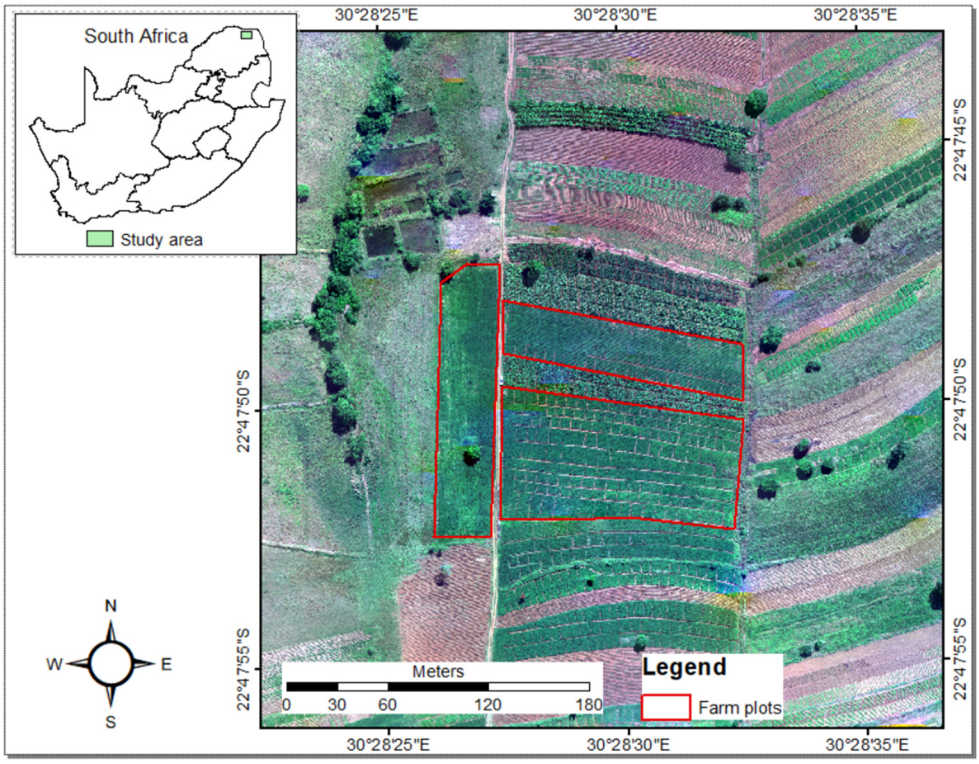


Figure 1. Study area map.

2.2. Data Acquisition

2.2.1. UAV Imagery Acquisition and Preparation

The DJI Metrics 600 Pro (M600) supplied by the SZ DJI Technology Co., Ltd., Shenzhen, China, was used in this study. The M600 was utilized as a platform at which the imaging sensor was used to acquire information about the sweet potato crop health condition in the study of interest. The M600 Pro was equipped with the A3 flight controller, ensuring a centimeter level positioning accuracy, 6 batteries, and gimbal. It had a remote controller with an operating frequency of 5.72 GHz and a transmission distance of 5 km. Table 1 shows the details of the UAV platform used in this study.

Table 1. UAV platform characteristics.

Platform	Items	Description
UAV	Weight	6 kg
	Altitude	120 m
	Area covered	16.34 hectares
	Flight time	15 min
	Speed	10 m/s
	Overlap	75%
	Side lap	75%
	Dimension	1.2 m
Red edge sensor	Bands	Blue, Green, Red, Red edge & NIR
	Focal length	5.5 mm
	Angle view	7.2 degrees
	Weight	150 g
	Image resolution	1280 mm × 960 mm
	Spatial resolution	8 cm

Prior to flying the UAV DJI Metrics 600 Pro (M600), the MicaSense Red-Edge multispectral camera (MicaSense, Inc., Seattle, WA, USA) mounted on the UAV platform was calibrated using the MicaSense Calibrated Reflectance Panel (CRP) (MicaSense, Inc., Seattle, WA, USA), readjusting the sensor with crop irradiance properties during the flight period.

Preprocessing was performed on the UAV multispectral images to correct for radiometric and geometric distortions that emanated during the crop fields scanning. The UAV images were preprocessed using the Drone2Map extension of the ArcGIS 10.8.1 software package. The orthorectification process was carried out to merge the raw image tiles for each spectral band to produce a single 2-dimensional image band in radiance based on the dark object subtraction (DOS) method. Moreover, the geometric correction process was carried out to spatially reference the orthomosaic image bands to the 1984 World Geodetic System (WGS84) based on Universal Transverse Mercator (UTM) zone 36S spheroid. We also converted digital number (Dn) of UAV imagery to radiance using Equation (1)

$$L = L_{min} + \left[\frac{Dn}{Dn_{max}} \times (L_{max} - L_{min}) \right] \quad (1)$$

where L denotes spectral radiance; L_{min} and L_{max} denote spectral radiance at $Dn = 0$ and spectral radiance at $Dn = max$ respectively, measured in milliwatts per square centimeter per steradian per micron (mW cm^{-2} sr^{-1} μm^{-1}).

2.2.2. Field Based and ASD Spectrometric Data

Through visual observation, a total of 71 points were surveyed to identify and sample deformed sweet potato leaves, and to measure their spectral signatures using the Analytical Spectra Device (ASD) field spectrometer (FieldSpec4 device) (Analytical Spectral Devices, Inc., Boulder, CO, USA). The purposive random sampling approach was used to select the samples from which spectral reflectance data for stressed or deformed leaves were collected. The locations on which leaf samples and their respective ASD spectral signatures were collected were recorded using the centimeter level precision Ashtech®ProMark2™ (Ashtech Inc., Santa Clara, CA, USA) Global Positioning System (GPS) device. Moreover, spectral signatures for healthy sweet potato leaves were measured and used as the threshold to determine the reflectance deviation of deformed leaves from healthy sweet potato leaves. The ASD field spectrometer utilized in this study measured the radiation reflected by sweet potato leaf within the spectral wavelength range of 350–2500 nm, i.e., the visible, near-infrared and shortwave-infrared spectral wavelengths. Prior to field hyperspectral measurements, cloudless weather conditions were considered to ensure that the spectral data were collected on sunny conditions. The ASD spectrometer was calibrated using the standard white panel radiance, to normalize the spectral reflectance patterns of the sampled crop leaves. During crop spectral data collection, the distance between the spectral gun and leaf samples was maintained at approximately 10 cm. Moreover, the crop leaf samples that exhibited stress or deformation were taken to the Agricultural Research Council, Mycology and Plant pathology laboratory, Pretoria, South Africa for disease diagnosis.

2.3. Hyperspectral Plotting of Healthy and Deformed Leaves

The spectral reflectance curves of infected sweet potato leaves, along with healthy sweet potato leaf, were plotted in the ViewSpec version 3.1.259 software package to visually analyze their reflectance properties across ranges of spectral wavelengths. The main purpose for this was to determine whether there were reflectance deviations of the deformed leaves from the healthy leaf, and whether there were reflectance deviations among the different types of leaf deformations. We also investigated whether sweet potato leaves exhibited unique reflectance in response to specific infection.

2.4. Analyzing Hyperspectral Reflectance of Infected Sweet Potato Leaves in Wavelengths Corresponding with UAV Spectral Bandwidths

In our study, we identified ASD spectral wavelengths that correspond with the UAV spectral bandwidths. This was done to satisfy our notion that, if there are differences in the reflectance of leaves infected with different diseases in the wavelengths corresponding with UAV spectral bandwidths, then the ASD reflectance data can be used to compute spatial configuration of different leaf infections on UAV imagery. We achieved this by converting hyperspectral reflectance data from the ".asd" format to the American Standard Code for Information Interchange (ASCII) in the ".txt" format using the OriginPro version 2021b software package. The reflectance values in ASCII format were arranged and organized in Microsoft Excel. Subsequently, the spectral curves of healthy and infected sweet potato leaves were plotted based on reflectance descriptive statistics computed from ASD wavelengths corresponding with UAV spectral bandwidths. Table 2 shows corresponding UAV spectral wavelengths used to extract reflectance data from ASD hyperspectral curves.

Table 2. The UAV spectral band information utilized to select corresponding ASD reflectance data.

Band Name	Wavelength Center (μm)	Wavelength Range (μm)
Blue	0.475	0.443–0.507
Green	0.56	0.533–0.587
Red	0.668	0.654–0.682
Red Edge	0.717	0.705–0.729
NIR	0.842	0.785–0.899

2.5. Assessing Variations in Hyperspectral Reflectance Across Different Crop Infection

Upon successful conversion of hyperspectral reflectance data to radiance format, the Levene k-comparison of equal variance test was deployed to determine whether variances in the radiance properties of different leaf deformations were equal. This was achieved using Equation (2) proposed by Levene [35]:

$$W = \frac{\left[(N-k)\sum_{i=1}^{k} N_i\left(\overline{Z}_{i.} - \overline{Z}.\right)^2\right]}{\left[(k-1)\sum_{i=1}^{k}\sum_{j=1}^{N_i}\left(Z_{ij} - \overline{Z}_{i.}\right)^2\right]} \quad (2)$$

where N is the sum of all samples from population groups (i.e., $n_1 + n_2 + n_3 + \ldots + n_t$); N_i is the number of sampled radiance data for each leaf deformation type; Z_{ij} is computed using Equation (3); k is the number of groups; and $Z..$ is the grand mean of all Z_{ij}, $i = 1, \ldots, k$, computed using Equation (5).

$$Z_{ij} = \left|Y_{ij} - \overline{Y}_i\right| \quad (3)$$

where Y_{ij} is the radiance value of i-th group; Y_i is the mean radiance value of the i-th group, computed using Equation (6).

$$\overline{Z}_i = \frac{1}{N_i}\sum_{i=1}^{N_i} Z_{ij} \quad (4)$$

$$\overline{Z}.. = \frac{1}{N}\sum_{i=1}^{k}\sum_{j=1}^{N_i} Z_{ij} \quad (5)$$

$$\overline{Y}_i = \frac{1}{N_i}\sum_{i=1}^{n_i} Y_{ij} \quad (6)$$

2.6. Analyzing Spectral Reflectance Overlaps in Identified Infected Leaves

In our study, we analyzed the reflectance overlap among the identified infected leaves across the ASD spectral wavelengths corresponding to UAV spectral bandwidths. Supposing that $f_1(x)$ and $f_2(x)$ denote the normal reflectance distribution with a common mean (μ) and undefined variances σ_1^2 and σ_2^2 respectively. Thus, common variance (C) can be computed as $\frac{\sigma_1}{\sigma_2}$, where $C > 0$. Thus, the overlap can be calculated as a function of C based on Equation (7) adopted from Mulekar and Mishra [36]:

$$\rho = \sqrt{\frac{2C}{1 + C^2}} \tag{7}$$

where ρ denotes overlap; and C denotes common variance between classes. Therefore, positive value indicates the presence of overlap in datasets, while negative and zero value denotes the absence of data overlap.

2.7. ASD Reflectance Threshold Selection for Spatially Characterizing Infected Leaves

Upon successful reflectance overlap analysis of deformed leaves, we adopted threshold optimization technique proposed by Mfamana and Ndou [23] to minimize overlap of datasets, such that

$$T_0 = \frac{(T_l + T_u)}{2} \tag{8}$$

where T_0 is the selected threshold; T_1 denotes the optimized threshold for the lower class; and T_u denotes the optimized threshold for the upper class. In this study, we applied the k-sigma technique to select thresholds for each class based on Equations (9) and (10) adopted from Bovenzi et al. [30]:

$$T_u = \mu + (k \times \sigma) \tag{9}$$

$$T_l = \mu - (k \times \sigma) \tag{10}$$

where T_u denotes upper threshold for a certain class; T_l denotes lower threshold μ and σ denote the mean standard deviation of the overlapping data respectively; and k is the parameter which is a positive integer. According to Laptev et al. [33], k is equal to 3 when data is assumed to be normally distributed.

2.8. Thresholding Classification of Infected Sweet Potato Crops

The minimum and maximum reflectance values obtained from the descriptive statistics results in the ASD spectral wavelengths for infected sweet potato crops that correspond with the UAV spectral wavelengths were used to spatially configure infected sweet potato crops on the UAV spectral indices by employing the bi-level thresholding segmentation classifier according to Kotte et al. [37], such that

$$L^T = \begin{cases} D_1 \leftarrow if\ T_{min_1} \leq L(x,y) \leq T_{max_1} \\ D_2 \leftarrow if\ T_{\min_2} \leq L(x,y) \leq T_{max_2} \\ D_3 \leftarrow if\ T_{min_3} \leq L(x,y) \leq T_{max_3} \\ D_4 \leftarrow if\ T_{min_4} \leq L(x,y) \leq T_{max_4} \\ 0,\ otherwise \end{cases} \tag{11}$$

where L^T denotes pixel in the x, y location; D denotes crop disease; T_{min} is the minimum reflectance threshold; and T_{max} is the maximum reflectance threshold.

2.9. Cross-Validation of Infected Sweet Potato Crops

The accuracy of infected sweet potato pattern generated using multilevel thresholding technique was evaluated using the validation datasets. We overlaid the GPS points for validation dataset on each UAV spectral band and extracted the pixel values on which the points were overlain, using the "Extract Values To Points" module embedded in the ArcMap version 10.8.2 software package. The extracted pixel radiance values were evaluated against the reflectance values computed from ASD reflectance data for deformed leaf samples. The coefficient of determination (Equation (12)) served to verify the accuracy of the predicted patterns:

$$R^2 = 1 - \frac{\sum_{i=1}^{N}\left(\hat{Y}_i - \overline{Y}_i\right)^2}{\sum_{i=1}^{N}\left(Y - \overline{Y}_1\right)^2} \quad (12)$$

where N denotes the number of samples; i is the variable i; Y_i denotes the measured reflectance data; $\hat{Y}_i$ denotes predicted radiance data; and $\overline{Y_1}$ denotes the mean value of dependent variable. The R^2 of at least 0.7 indicates an accurate pattern prediction, while R^2 value below 0.7 indicates an imprecise pattern.

2.10. Areal Determination of Infected Sweet Potato Crops

Upon the successful spatial configuration of infected sweet potato crops from the UAV imagery, its area was computed based on Equation (13):

$$AREA_{(\%)} = \frac{\sum_{i=1}^{n} P_{(i_{sp})}}{\sum_{i=1}^{n} P_I} \times 100 \quad (13)$$

where $P_{(d_{sp})}$ denotes pixels for infected sweet potato; and P_I denotes pixels for the entire image.

3. Results

3.1. Diagnostic Results of Sweet Potato Deformed Leaves

Laboratory analysis results of the sampled deformed sweet potato leaves revealed various causes of leaf deformation. Table 3 shows the sampled leaves and their respective diagnostic results.

Table 3. Leaf samples and their corresponding diagnostic results.

Leaf Sample	Diagnosis	Description
	Nutrient deficient	Yellow to brown which is stunted due to insufficient nutrients which may be caused by leaching from heavy rains, irrigation, low organic matter or insufficient fertilization.
	SPVC-positive	Yellow mottling, purpling, vein clearing, stunting and chlorotic blotches or spot.
	Old leaf	Yellow to brown color which may be a sign of decay. The results show that these samples are in the process of decomposing, as they may be less nutritious.
	Fungi isolates: *Alternaria*, *Bipolaris*, *Fusarium*, *Phoma*	Small brown spots on the leaves, surrounded by a yellow or reddish halo, wilting and brown lesions.

Table 3. *Cont.*

Leaf Sample	Diagnosis	Description
	Insect damage: Insect damage. Possibly morning glory leaf miner (*Bedellia somnulentella*) or sweet potato growth point caterpillar (*Hydris ornatalis*)	Samples showed brown to blackish spots, wilting deformed leaves.
	Mechanically damaged	Yellow to brown color symptoms which may provide entry point for insects and pathogens.

Laboratory diagnostic results of 54 surveyed deformed sweet potato crop leaves confirmed the following causes of leaf deformation: (a) nutrient deficiency (ND); (b) SPVC-positive (SPVC); (c) old leaf (OL); (d) fungi isolate (FI), which included *Alternaria*, *Bipolaris*, *Fusarium* and *Phoma*; (e) insect damage (ID); and (f) mechanical damage (MD). Fungi-related diseases such as *Alternaria* are characterized by brown lesions with a typical appearance of concentric rings. *Curvularia* and *Phoma* fungi were associated with small, light-brown, irregular-shaped leaf spots.

3.2. Hyperspectral Reflectance Analysis of Deformed Leaves in the Wavelengths Corresponding to UAV Spectral Bands

Spectral reflectance patterns of deformed sampled leaves were plotted and analyzed against the healthy leaf sample, based on the ASD spectral wavelengths corresponding with UAV multispectral sensor used in this study. Figure 2 provides spectral reflectance curves of a healthy sweet potato leaf against a leaf that exhibited different types of deformation.

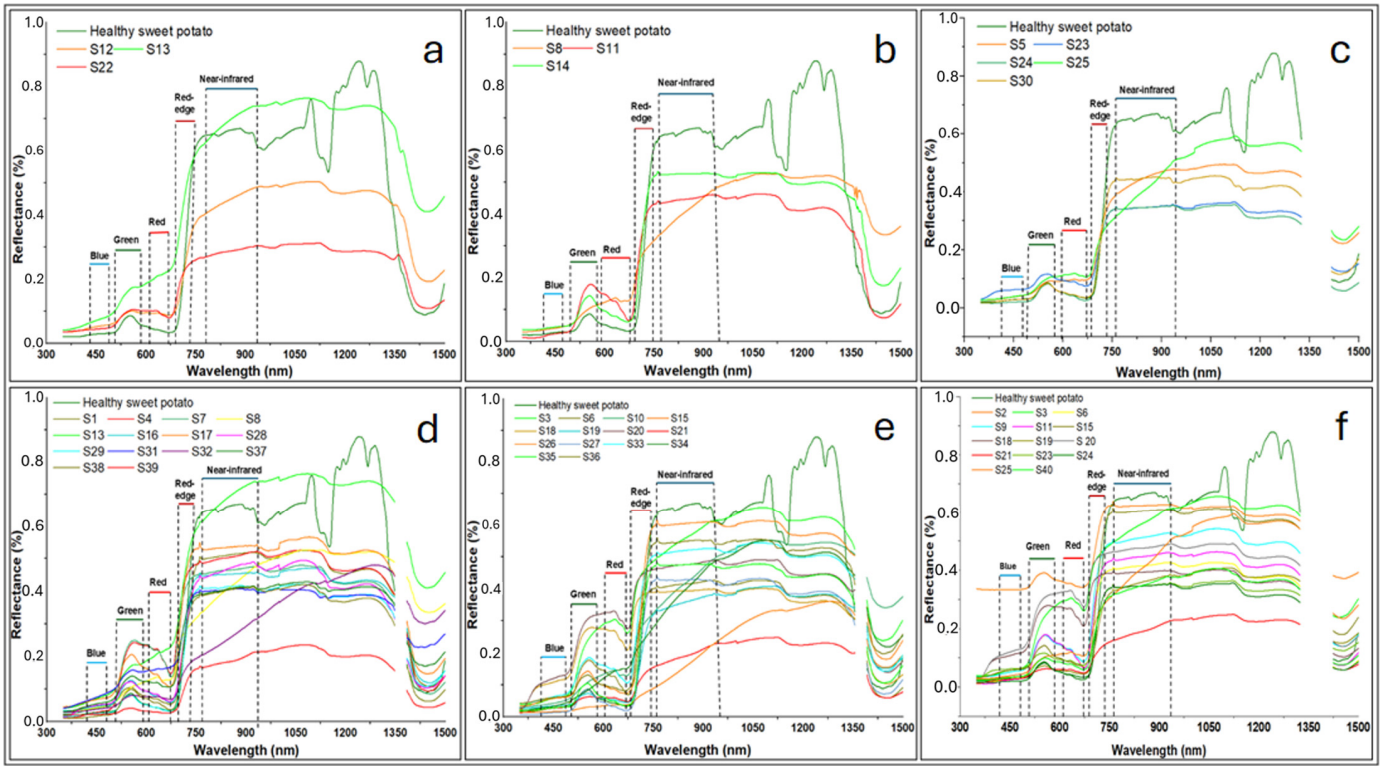


Figure 2. Spectral reflectance curve of healthy sweet potato leaf against (**a**) nutrient-deficient, (**b**) SPVC-infected, (**c**) old leaf, (**d**) fungi-infected, (**e**) insect-damage, and (**f**) mechanically damaged leaf.

Since the focus of the study was to integrate ASD hyperspectral reflectance data into UAV multispectral imagery, we only focused on the wavelengths of ASD spectrometer which correspond with UAV's discrete spectral bands. Generally, the majority of leaf samples for all deformation types exhibited higher reflectance than a healthy leaf in the visible spectral region (i.e., blue, green, red and red edge corresponding UAV spectral bands), and lower reflectance than the healthy sample in the NIR spectral wavelength. Despite this, variability in reflectance among leaf samples of the same deformation type was also noted. Detailed data regarding variability in reflectance of surveyed samples is provided in Section 3.3 of this manuscript.

3.3. Levene's Statistical Results for ASD-Based Leaf Sample Reflectance Variability Analysis

Levene's statistical results computed from the reflectance data from the ASD spectrometric wavelength corresponding with spectral bands of a UAV multispectral sensor for leaf samples are presented in this study (Table 4).

Table 4. Levene's k-comparison of equal variance statistics for sample radiance variability obtained from ASD wavelengths corresponding with UAV sensor.

	0.443–0.507 µm							0.533–0.587 µm						
	ND	SPVC	OL	FI	ID	MD	HL	ND	SPVC	OL	FI	ID	MD	HL
N	3	3	5	14	14	14	5	3	3	5	14	14	14	5
Min.	0.028	0.024	0.020	0.016	0.012	0.02	0.028	0.089	0.088	0.056	0.033	0.027	0.269	0.056
Max.	0.101	0.061	0.076	0.097	0.165	0.165	0.035	0.178	0.18	0.117	0.049	0.279	0.391	0.086
$\bar{x}$	0.061	0.132	0.186	0.052	0.054	0.076	0.030	0.122	0.134	0.087	0.13	0.138	0.167	0.075
σ	0.006	0.006	0.003	0.005	0.005	0.005	0.002	0.005	0.011	0.007	0.002	0.01	0.009	0.010
p-value				0.048							0.052			
	0.654–0.682 µm							0.705–0.729 µm						
	ND	SPVC	OL	FI	ID	MD	HL	ND	SPVC	OL	FI	ID	MD	HL
N	3	3	5	14	14	14	5	3	3	5	14	14	14	5
Min.	0.087	0.062	0.025	0.033	0.019	0.025	0.033	0.164	0.127	0.129	0.129	0.061	0.105	0.129
Max.	0.243	0.14	0.103	0.243	0.301	0.343	0.037	0.526	0.421	0.425	0.495	0.464	0.59	0.425
$\bar{x}$	0.133	0.09	0.059	0.101	0.114	0.132	0.035	0.304	0.298	0.254	0.309	0.299	0.325	0.268
σ	0.004	0.002	0.002	0.004	0.004	0.005	0.001	0.035	0.047	0.054	0.044	0.035	0.032	0.033
p-value				0.061							0.071			
	0.785–0.899 µm													
	ND	SPVC	OL	FI	ID	MD	HL							
N	3	3	5	14	14	14	5							
Min.	0.271	0.352	0.034	0.169	0.111	0.324	0.648							
Max.	0.726	0.527	0.669	0.517	0.608	0.622	0.654							
$\bar{x}$	0.47	0.458	0.448	0.434	0.43	0.417	0.651							
σ	0.018	0.011	0.006	0.01	0.011	0.003	0.002							
p-value				0.102										

At $\alpha = 0.05$, the *p*-value computed to evaluate variability in mean radiance properties for deformed leaf samples in 0.443–0.507 µm, 0.533–0.587 µm, 0.654–0.682 µm, 0.705–0.729 µm and 0.785–0.899 µm wavelengths were noted to be 0.048, 0.052, 0.061, 0.071 and 0.102 respectively. This implies that various leaf deformation types can be distinguished based on the blue spectral band of the UAV multispectral sensor. We then used the mean reflectance values in Table 4 to plot the mean reflectance profile for different leaf deformation types (Figure 3).

Visual interpretation of Figure 3 revealed a clear distinction between deformed leaves and a healthy leaf in all but the red edge spectral wavelength. Moreover, there were no clear distinctions among different types of leaf deformation. However, Figure 3 shows that

old leaf (OL) SPVC can be distinguished from other deformation types in the blue spectral channel (0.443–0.507 µm). Old leaf can also be distinguished in green, red and red edge spectral channels.

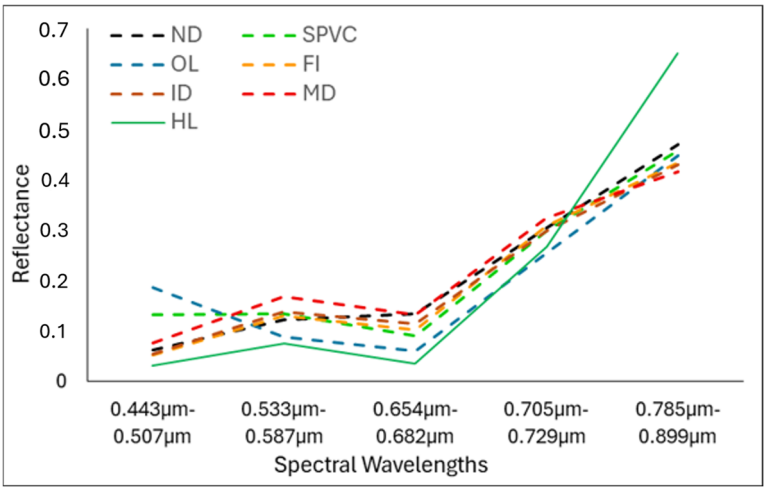


Figure 3. Mean radiance properties for different leaf deformation types.

3.4. Reflectance Overlap Analysis of Various Leaf Deformation Types

In order to analyze spectral reflectance overlap among leaf deformation types, we started by computing the C-coefficient of variance as shown in Table 5.

Table 5. The C-coefficient values attained from cross-computation of variances for different leaf deformation types.

	0.443–0.507 µm							0.533–0.587 µm						
	ND	SPVC	OL	FI	ID	MD	HL	ND	SPVC	OL	FI	ID	MD	HL
ND	-	1.0	2.0	1.2	1.2	1.2	3.0	-	0.46	0.71	2.5	0.5	0.56	0.5
SPVC	1.0	-	2.0	1.2	1.2	1.2	3.0	2.2	-	1.57	5.5	1.1	1.22	1.1
OL	0.5	0.5	-	0.6	0.6	0.6	1.5	1.4	0.06	-	3.5	0.7	0.78	0.7
FI	0.83	0.83	1.67	-	1	1	2.5	0.4	0.18	0.29	-	0.2	0.22	0.2
ID	0.83	0.83	1.67	1	-	1	2.5	2	0.91	1.43	5	-	1.11	1
MD	0.83	0.83	1.67	1	1	-	2.5	0.18	0.82	1.29	4.5	0.9	-	0.9
HL	0.33	0.33	0.67	0.4	0.4	0.4	-	2	0.91	1.43	5	1	1.11	-
	0.654–0.682 µm							0.705–0.729 µm						
	ND	SPVC	OL	FI	ID	MD	HL	ND	SPVC	OL	FI	ID	MD	HL
ND	-	2	2	1	1	0.8	4	-	0.74	0.67	0.8	1	1.09	0.38
SPVC	0.05	-	1	0.05	0.05	0.4	1	1.34	-	0.87	1.07	1.34	1.47	0.51
OL	0.05	1	-	0.05	0.05	0.4	1	1.54	1.15	-	1.23	1.54	1.69	0.06
FI	1	2	2	-	1	0.8	4	1.26	0.94	0.82	-	1.26	1.38	0.05
ID	1	2	2	1	-	0.8	4	1	0.74	0.67	0.8	-	1.09	0.38
MD	0.13	2.5	2.5	0.13	0.13	-	5	0.92	0.68	0.59	0.07	0.92	-	0.03
HL	0.25	0.5	0.5	0.25	0.25	0.2	-	0.003	1.99	1.72	2.11	0.003	2.91	-
	0.785–0.899 µm													
	ND	SPVC	OL	FI	ID	MD	HL							
ND	-	1.64	3	1.8	1.64	6	9							
SPVC	0.61	-	1.83	1.1	1	3.67	0.5							
OL	0.33	0.55	-	.6	0.55	2	3							
FI	0.56	0.91	1.67	-	0.91	3.33	5							
ID	0.61	1	1.83	1.1	-	3.67	0.5							
MD	0.17	0.27	0.5	0.3	0.27	-	1.5							
HL	0.11	0.18	0.33	0.2	0.18	0.67	-							

The second step after the computation of the C-coefficient was to determine the actual spectral reflectance overlap across the leaf deformation types as shown in Table 6.

Table 6. Reflectance overlap among leaf deformation types.

	0.443–0.507 µm							0.533–0.587 µm						
	ND	SPVC	OL	FI	ID	MD	HL	ND	SPVC	OL	FI	ID	MD	HL
ND	-	0.71	0.89	0.99	0.99	0.99	0.78	-	0.87	0.97	0.83	0.89	0.92	0.89
SPVC	1	-	0.89	0.99	0.99	0.99	0.78	0.87	-	0.95	0.59	0.99	0.99	0.99
OL	0.89	0.89	-	0.94	0.94	0.94	0.96	0.98	0.35	-	0.73	0.97	0.99	0.97
FI	0.99	0.89	0.94	-	1	1	0.83	0.83	0.59	0.73	-	0.62	0.65	0.62
ID	0.99	0.89	0.94	1	-	1	0.83	0.89	0.99	0.97	0.62	-	0.99	1
MD	0.99	0.89	0.94	1	1	-	0.83	0.59	0.99	0.98	0.65	0.99	-	0.99
HL	0.77	0.89	0.96	0.83	0.831	0.939	-	0.89	0.99	0.97	0.62	1	0.99	-
	0.654–0.682 µm							0.705–0.729 µm						
	ND	SPVC	OL	FI	ID	MD	HL	ND	SPVC	OL	FI	ID	MD	HL
ND	-	0.89	0.89	1	1	0.99	0.69	-	0.98	0.97	0.99	1	1.0	0.82
SPVC	0.32	-	1	0.32	0.32	0.83	1	0.98	-	0.99	1.0	0.98	0.96	0.9
OL	0.32	1	-	0.32	0.32	0.83	1	0.96	0.99	-	1.0	0.99	0.94	0.35
FI	1	0.89	0.89	-	1	0.99	0.69	0.99	0.99	0.99	-	0.99	0.98	0.32
ID	1	0.89	0.89	1	-	0.99	0.69	1	0.98	0.96	0.99	-	1.0	0.82
MD	0.51	0.83	0.83	0.51	0.51	-	0.62	0.99	0.96	0.94	0.37	1.0	-	0.25
HL	0.69	0.89	0.89	0.69	0.69	0.62	-	0.08	0.9	0.93	0.88	0.08	0.78	-
	0.785–0.899 µm													
	ND	SPVC	OL	FI	ID	MD	HL							
ND	-	0.94	0.78	0.92	0.94	0.57	0.47							
SPVC	0.94	-	0.92	1.0	1	0.71	0.89							
OL	0.77	0.92	-	0.57	0.92	0.89	0.78							
FI	0.92	1.0	0.94	-	1.0	0.74	0.62							
ID	0.94	1	0.92	1.0	-	0.71	0.89							
MD	0.56	0.71	0.89	0.74	0.71	-	0.96							
HL	0.47	0.59	0.77	0.62	0.59	0.96	-							

From Table 6, the reflectance overlap was noted among all the leaf deformation types, i.e., all leaf deformation types showed values greater than 0, which indicated the presence of overlaps.

Determination of thresholds among leaf deformation types.

Due to reflectance overlap across different leaf deformation types, optimizing the selection of inter-class threshold values was necessary in this study. Table 7 provides the lower and upper k-sigma thresholds computed to optimize the spectral separation of different leaf deformation types.

In a 0.443–0.507 µm spectral wavelength, reflectance properties for a leaf with nutrient deficiency overlapped with a leaf infected with fungi isolates, insect damage, mechanical damage and a healthy leaf. In a 0.654–0.682 µm wavelength, ND, MD, ID and FI were also found, with SPVC and FI as well. In 0.533–0.587 µm, 0.705–0.729 µm and 0.785–0.899 µm spectral wavelengths, reflectance overlaps were noted across all leaf deformation types. Figure 4 shows graphs depicting minimum and maximum reflectance thresholds for each sweet potato leaf deformation type.

From Figure 4, reflectance overlap was apparent in many spectral wavelengths. While some leaf deformation types showed discrepancies in their respective minimum and maximum reflectance, it is not possible to spectrally distinguish them because their ranges fall within the same spectrum, i.e., the minimum value of one class does not start after the maximum values of another class and vice versa.

Table 7. The k-sigma thresholds for distinguishing leaf deformation types.

	0.443–0.507 µm		0.533–0.587 µm		0.654–0.682 µm		0.705–0.729 µm		0.785–0.899 µm	
	T_l	T_u	T_l	T_u	T_l	T_u	T_l	T_u	T_l	T_u
ND	0.043	0.079	0.107	0.137	0.121	0.145	0.199	0.445	0.416	0.524
SPVC	0.114	0.15	0.101	0.167	0.084	0.096	0.157	0.439	0.425	0.491
OL	0.177	0.195	0.066	0.108	0.053	0.065	0.092	0.416	0.43	0.466
FI	0.037	0.067	0.124	0.136	0.089	0.113	0.177	0.441	0.404	0.464
ID	0.039	0.069	0.108	0.168	0.102	0.126	0.194	0.404	0.397	0.463
MD	0.061	0.091	0.14	0.194	0.117	0.182	0.229	0.421	0.408	0.426
HL	0.024	0.036	0.045	0.178	0.032	0.038	0.169	0.547	0.645	0.657

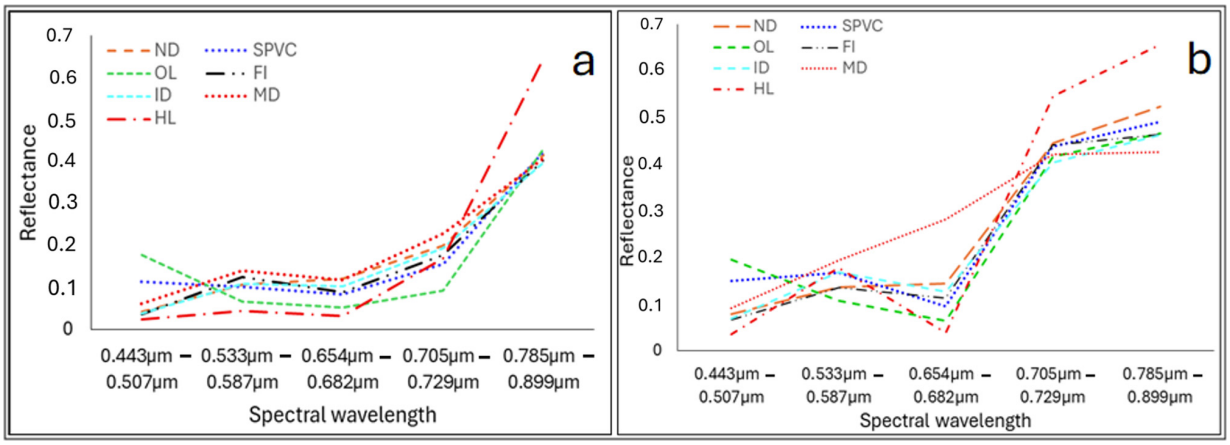


Figure 4. Established (**a**) minimum thresholds and (**b**) maximum thresholds for leaf deformation types.

3.5. Spatial Configuration of Infected Sweet Potato Crop

Upon successful derivation of minimum and maximum values for each spectral vegetation index from descriptive statistics, results generated from ASD wavelengths for infected sweet potato crop were produced (Figure 5).

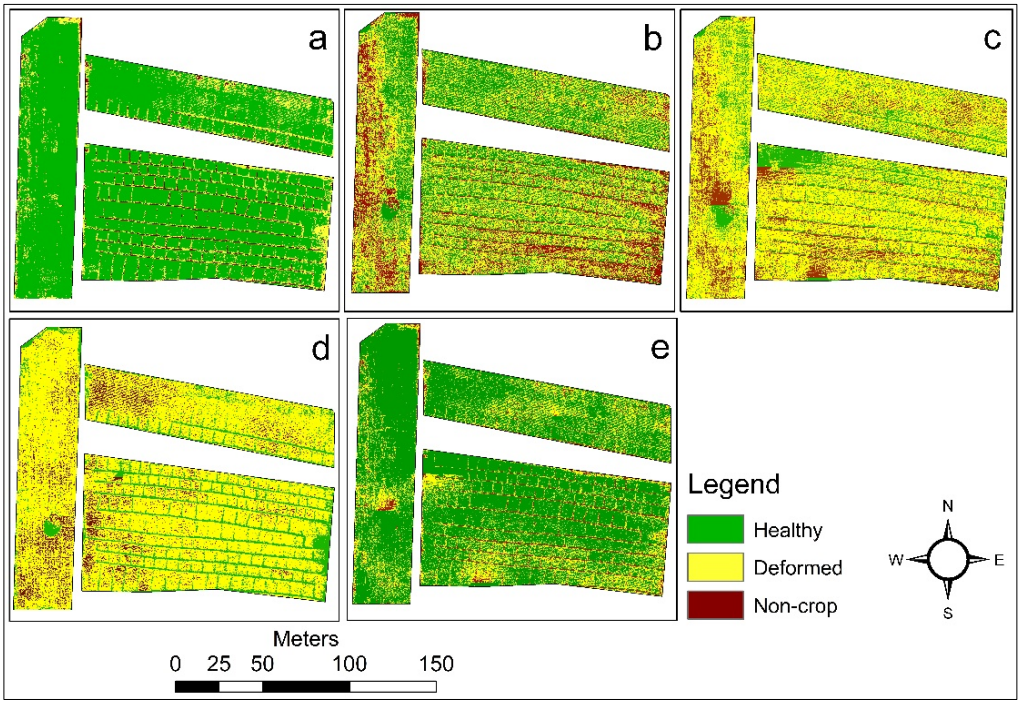


Figure 5. Spatial variability in deformed leaves as predicted by thresholding (**a**) blue, (**b**) green, (**c**) red, (**d**) red edge and (**e**) NIR spectral bands.

3.6. Accuracy Evaluation of Infected Sweet Potato Pattern

Accuracy of the predicted deformed sweet potato leaves from UAV imagery based on ASD spectral reflectance data was evaluated. Table 8 shows the coefficient of determination results for predicted spatial patterns in deformed sweet potato leaves.

Table 8. The coefficient of determination results for validating classified image.

Spectral Band	R^2
Blue	0.23
Green	0.19
Red	0.28
Red edge	0.17
NIR	0.63

The coefficient of determination technique for validating deformed sweet potato leaf class generally yielded poor classification results, with R^2 value of 0.23, 0.19, 0.28, 0.17 and 0.63 for blue, green, red, red edge and NIR respectively. However, multilevel thresholding of deformed sweet potato leaves in NIR spectral band yielded R^2 results that are far better than with other spectral bands (Table 8).

3.7. Areal Analysis of Deformed Leaves

The area occupied by deformed sweet potato leaves as predicted by thresholding of UAV spectral bands are presented in Table 9.

From Table 9, the quantified area covered by deformed sweet potato leaves were noted to be 11.91%, 28.71%, 43.66%, 46.41% and 30.6% for blue, green, red, red edge and NIR respectively. Generally, the misclassification of deformed sweet potato leaves was noted in all UAV spectral bands.

Table 9. Area covered by infected sweet potato crops from thresholding of spectral bands.

	Area (%)				
	Blue	**Green**	**Red**	**Red-Edge**	**NIR**
Non-crop	4.66	33.11	25.07	34.66	11.7
Deformed leaves	11.91	28.71	43.66	46.41	30.6
Heathy leaves	83.43	38.18	31.27	18.93	58.3

4. Discussion

Crop diseases constitute a significant constraint to sweet potato production in small-scale farms [38]. However, accurate determination of spatial patterns in sweet potato crop diseases is challenging when carried out using a conventional field inspection method. In this study, we investigated the prospect of spatially partitioning the UAV imagery to uncover spatial distribution of infected sweet potato crops by using hyperspectral reflectance data acquired from the ASD field spectrometer. The information on crop conditions acquired through remote sensing technology offers invaluable information on crop production and yield estimates [39]. According to the results obtained from the current study, our discussion is structured to address the subsequent questions:

- What are the general conditions of sweet potato crops?
- What are the causes of the deformation of sweet potato leaves in the experimental site?
- To what extent can UAV multispectral imagery and non-imaging hyperspectral data spectrally characterize sweet potato diseases?

- How effective is the multi-value thresholding segmentation classifier in spatially partitioning infected sweet potato crop?

The identification of deformed leaf samples followed a multi-stage approach. Visual inspection was initially used to identify deformed leaves in the field for sampling purposes. These samples were then subjected to laboratory analysis to determine the specific causes of deformation. Spectral reflectance disparities between the deformed samples and the healthy leaf were analyzed. The classification of UAV imagery was subsequently performed using ASD-derived spectral thresholds rather than visual interpretation. The laboratory analysis results of the diagnosed leaf samples revealed nutrient deficiency, SPVC, insect damage, mechanical damage and fungi isolation as the factors affecting sweet potato crops. Mulabisana et al. [40] also noted the frequent occurrence of SPVC in the Dzimauli small-scale farms. Mechanically damaged leaves are attributed to recurrent weed removal process during different crop growth stages. Wright et al. [41] and Patel et al. [42] also noted that laboratory diagnostic technique is a useful screening method for evaluating the susceptibility of sweet potato to infection. However, this approach has limitations as it is expensive, time consuming and may delay disease response. Although these limitations are common when using this approach, this approach provides more accurate point-based information regarding crop conditions than other approaches such as remote sensing, which still requires validation using the same laboratory technique.

The results obtained from non-imaging field spectrometry revealed high reflectance of all leaf deformation types in the green (500–600 nm), and red (600–700 nm) bands, and low reflectance in the near-infrared (700–1300 nm) when compared to healthy sweet potato leaf (Figure 2). By implications, these spectral wavelengths can be used in differentiating deformed sweet potato leaves from healthy ones. Nkuna et al. [2] noted that disease severity in crops can be characterized by analyzing deviation of spectral reflectance between healthy and infected crops. However, construction of spatial continuity in crop deformed leaves using non-imaging hyperspectral remote sensing technology is a challenging task. This was supported by Bai et al. [43] who stated that although hyperspectral remote sensing techniques are important in crop disease detection, studies still emphasize the need to advance this approach from different perspectives.

It is important to note that the thresholds used in this study were not predefined prior to classification. Instead, they were derived from descriptive statistics of ASD spectral reflectance data collected from laboratory-confirmed leaf deformation types. This ensured that the threshold values used in the classification process were empirically based and representative of actual crop infection conditions. However, the overlap results revealed spectral overlaps across almost all the surveyed leaf deformation types. This constrained the spatial configuration of sweet potato crops based on leaf deformation types. Instead, sweet potato crops were generally segmented by applying minimum and maximum reflectance values of the entire dataset. Although studies noted the efficacy of mean spectral reflectance values as threshold [44,45], this approach tends to undermine variations in crop reflectance as result of varying illumination intensity [23]. Moreover, it must be noted that a framework for facilitating both the selection of the most suitable thresholding method for a particular domain and the application of thresholds to facilitate the classification of spectrally overlapping crops is unavoidable. Results obtained from this study showed that, despite the optimization of thresholds through the k-sigma technique, spatial partitioning of various sweet potato leaf deformations is a challenging issue [46]. Moreover, overlapping cases often exist in the proximity of the decision boundary [47], making the learning process a major issue [48].

The inability to spatially partition sweet potato crops based on leaf deformation types could be attributed to a lack of a clear framework for detecting infection-related

hyperspectral features, coupled by a lack of practical case studies [49]. For instance, a virus can cause leaf damage by degrading pigment and wilting a leaf structure, which may subsequently cause nutrient deficiencies [50]. This makes it difficult to spectrally distinguish nutrient deficit-related spectral signature from spectral signatures of a leaf affected by some viruses and bacteria. Furthermore, the temporal dimension of disease symptoms in crops is important and must be considered during crop disease monitoring process. Whereas short-term diseases often exhibit changes in photosynthetic, respiratory and transpiration potential of a leaf, long-term diseases may have more persistent impact on crop growth and development [51]. Kranner et al. [52] also noted that crop response to infection often exhibits nonlinear patterns.

Because UAV systems normally take more time to scan the ground when compared with satellite systems, different UAV image tiles may be subjected to different turbulence, different incidence angles, different illumination, or different signal processing chains [53,54]. Therefore, integration of these variables in infected crop classification is recommended. In the current study, effects of these variables on the reflectance quality of deformed leaves were not considered, necessitating them as a direction for future study. Haralick et al. [55] showed that combining spectral information with texture features can further enhance the accuracy of classification. We encourage that future studies evaluate the efficacy of other thresholding optimization techniques in handling leaf deformation types with reflectance overlaps. This is because various types of crops exhibit unique textural properties [48] regardless of similarity in their spectral properties. This distinct textural characteristic plays an important role in distinguishing different land features that exhibit significant similar spectral properties [20]. Against the backdrop provided, issues that emanated from the findings of this study underscores the need to further pursue alternative approaches for spectrally distinguishing various causes of sweet potato leaf deformation.

5. Conclusions

The study aimed to search for a framework for mapping infected sweet potato crops by integrating the ASD spectrometric data into UAV imagery. The study noted that thresholding of UAV imagery based on ASD spectrometric data does not yield accurate classification results. Multilevel thresholding results of UAV spectral bands revealed varying patterns of causes of sweet potato leaf deformation. The overlap results revealed spectral overlaps among all the causes of sweet potato leaf deformation. The coefficient of determination results showed that the thresholding of the UAV NIR spectral band produced results that are close to accuracy. It may be interesting to analyze crop infection at different crop growing stages such as vegetative, tasseling and maturity stages. Future research must attempt to distinguish stressed sweet potato crops due to infection from stressed sweet potato crops due to other stressors such as nutrient deficiency, water, pathogens, etc. Finally, this study demonstrated the ongoing importance of remote sensing technology in addressing challenges related to crop health and yield, and subsequently the contribution to the global food security goal.

Author Contributions: Conceptualization, N.N. and A.N.; methodology, S.F.; software, N.N. and S.F.; validation, N.N. and A.N.; formal analysis, S.F.; investigation, N.N. and S.F.; resources, A.N.; writing—original draft preparation, N.N.; writing—review and editing, N.N.; project administration, A.N.; funding acquisition, A.N. All authors have read and agreed to the published version of the manuscript.

Funding: This study was funded by the National Research Foundation (NRF), Grant number (UID): 129886.

Institutional Review Board Statement: Not applicable.

Informed Consent Statement: Not applicable.

Data Availability Statement: The raw data supporting the conclusions of this article will be made available by the authors on request.

Conflicts of Interest: The authors declare no conflicts of interest.

References

1. Loebenstein, G.; Fuentes, S.; Cohen, J.; Salazar, L.F. Sweet Potato. In *Virus and Virus-like Diseases of Major Crops in Developing Countries*; Loebenstein, G., Thottappilly, G., Eds.; Springer: Dordrecht, The Netherlands, 2003. [CrossRef]
2. Nkuna, B.L.; Chirima, J.G.; Newete, S.W.; Nyamugama, A.; van der Walt, A.J. Developing models to detect maize diseases using spectral vegetation indices derived from spectral signatures. *Egypt. J. Remote Sens. Space Sci.* **2024**, *27*, 597–603. [CrossRef]
3. Thompson, G.J.; Domola, M.J. Viral diseases. In *Guide to Sweet Potato Production in South Africa*; Niederwieser, J.G., Ed.; ARC-Roodeplaat Vegetable and Ornamental Plant Institute: Roodeplaat, South Africa, 2004; pp. 77–80.
4. Wang, L.; Poque, S.; Valkonen, J.P. Phenotyping viral infection in sweet potato using a high-throughput chlorophyll fluorescence and thermal imaging platform. *Plant Methods* **2019**, *15*, 116. [CrossRef] [PubMed]
5. Deka, D.; Rabha, J.; Jha, D.K. Application of Myconanotechnology in the sustainable management of crop production system. *Mycoremediat. Environ. Sustain.* **2018**, *2*, 273–305. [CrossRef] [PubMed]
6. Donatelli, M.; Magarey, R.D.; Bregaglio, S.; Willocquet, L.; Whish, J.P.; Savary, S. Modelling the impacts of pests and diseases on agricultural systems. *Agric. Syst.* **2017**, *155*, 213–224. [CrossRef] [PubMed]
7. Lowe, A.; Harrison, N.; French, A.P. Hyperspectral image analysis techniques for the detection and classification of the early onset of plant disease and stress. *Plant Methods* **2017**, *13*, 80. [CrossRef] [PubMed]
8. Feng, W.; Qi, S.; Heng, Y.; Zhou, Y.; Wu, Y.; Liu, W.; He, L.; Li, X. Canopy vegetation indices from in-situ hyperspectral data to assess plant water status of winter wheat under powdery mildew stress. *Front. Plant Sci.* **2017**, *8*, 1219. [CrossRef] [PubMed]
9. Feng, Z.H.; Wang, L.Y.; Yang, Z.Q.; Zhang, Y.Y.; Li, X.; Song, L.; He, L.; Duan, J.Z.; Feng, W. Hyperspectral Monitoring of Powdery Mildew Disease Severity in Wheat Based on Machine Learning. *Front. Plant Sci.* **2022**, *13*, 828454. [CrossRef] [PubMed]
10. Franceschini, A.; Foffano, L.; Prandini, E.; Tavecchio, F. Very high-energy constraints on the infrared extragalactic background light. *Astron. Astrophys.* **2019**, *629*. [CrossRef]
11. Cordon, G.; Andrade, C.; Barbara, L.; Romero, A.M. Early detection of tomato bacterial canker by reflectance indices. *Inf. Process. Agric.* **2022**, *9*, 184–194. [CrossRef]
12. Feng, Z.; Song, L.; Duan, J.; He, L.; Zhang, Y.; Wei, Y.; Feng, W. Monitoring wheat powdery mildew based on hyperspectral, thermal infrared, and RGB image data fusion. *Sensors* **2021**, *22*, 31. [CrossRef] [PubMed]
13. Wan, L.; Li, H.; Li, C.; Wang, A.; Yang, Y.; Wang, P. Hyperspectral sensing of plant diseases: Principle and methods. *Agronomy* **2022**, *12*, 1451. [CrossRef]
14. Retkute, R.; Crew, K.S.; Thomas, J.E.; Gilligan, C.A. Detection of Banana Diseases Based on Landsat-8 Data and Machine Learning. *Remote Sens.* **2025**, *17*, 2308. [CrossRef]
15. Roy, D.P.; Wulder, M.A.; Loveland, T.R.; Woodcock, C.E.; Allen, R.G.; Anderson, M.C.; Helder, D.; Irons, J.R.; Johnson, D.M.; Kennedy, R.; et al. Landsat-8: Science and product vision for terrestrial global change research. *Remote Sens. Environ.* **2014**, *145*, 154–172. [CrossRef]
16. Fu, H.; Zhao, H.; Song, R.; Yang, Y.; Li, Z.; Zhang, S. Cotton aphid infestation monitoring using Sentinel-2 MSI imagery coupled with derivative of ratio spectroscopy and random forest algorithm. *Front. Plant Sci.* **2022**, *13*, 1029529. [CrossRef] [PubMed]
17. Yang, X. Identification and Monitoring of Crop Pests and Diseases Based on Remote Sensing Technology. *Trans. Environ. Energy Earth Sci.* **2024**, *3*, 130–136. [CrossRef]
18. Milas, A.S.; Arend, K.; Mayer, C.; Simonson, M.A.; Mackey, S. Different colours of shadows: Classification of UAV images. *Int. J. Remote Sens.* **2017**, *38*, 3084–3100. [CrossRef]
19. Gao, J.; Gujarati, K.; Hegde, M.; Arra, P.; Gupta, S.; Buch, N. Integration of UAV and Remote Sensing Data for Early Diagnosis and Severity Mapping of Diseases in Maize Crop Through Deep Learning and Reinforcement Learning. *Remote Sens.* **2025**, *17*, 3427. [CrossRef]
20. Shahi, T.B.; Xu, C.-Y.; Neupane, A.; Guo, W. Recent Advances in Crop Disease Detection Using UAV and Deep Learning Techniques. *Remote Sens.* **2023**, *15*, 2450. [CrossRef]
21. Zhang, N.; Yang, G.; Pan, Y.; Yang, X.; Chen, L.; Zhao, C. A review of advanced technologies and development for hyperspectral-based plant disease detection in the past three decades. *Remote Sens.* **2020**, *12*, 3188. [CrossRef]
22. Thomas, S.; Kuska, M.T.; Bohnenkamp, D.; Brugger, A.; Alisaac, E.; Wahabzada, M.; Mahlein, A.K. Benefits of hyperspectral imaging for plant disease detection and plant protection: A technical perspective. *J. Plant Dis. Prot.* **2018**, *125*, 5–20. [CrossRef]
23. Mfamana, S.; Ndou, N. Evaluation of Multilevel Thresholding in Differentiating Various Small-Scale Crops Based on UAV Multispectral Imagery. *Appl. Sci.* **2025**, *15*, 10056. [CrossRef]

24. Wani, J.A.; Sharma, S.; Muzamil, M.; Ahmed, S.; Sharma, S.; Singh, S. Machine learning and deep learning based computational techniques in automatic agricultural diseases detection: Methodologies, applications, and challenges. *Arch. Comput. Methods Eng.* **2022**, *29*, 641–677.
25. Ewees, A.A.; Abualigah, L.; Yousri, D.; Sahlol, A.T.; Al-qaness, M.A.A.; Alshathri, S.; Elaziz, A. Modified Artificial Ecosystem-Based Optimization for Multilevel Thresholding Image Segmentation. *Mathematics* **2021**, *9*, 2363. [CrossRef]
26. Hernández Molina, D.D.; Gulfo-Galaraga, J.M.; López-López, A.M.; Serpa-Imbett, C.M. Methods for estimating agricultural cropland yield based on the comparison of NDVI images analyzed by means of Image segmentation algorithms: A tool for spatial planning decisions. *Ingeniare Rev. Chil. Ing.* **2023**, *31*, 24. [CrossRef]
27. Hosny, K.M.; Khalid, A.M.; Hamza, H.M.; Mirjalili, S. Multilevel thresholding satellite image segmentation using chaotic coronavirus optimization algorithm with hybrid fitness function. *Neural Comput. Appl.* **2023**, *35*, 855–886. [PubMed]
28. Tukey, J.W. *Exploratory Data Analysis*; Addison-Wesley: Reading, MA, USA, 1977; Volume 2.
29. Bovenzi, G.; Aceto, G.; Ciuonzo, D.; Montieri, A.; Persico, V.; Pescapé, A. Network anomaly detection methods in IoT environments via deep learning: A fair comparison of performance and robustness. *Comput. Secur.* **2023**, *128*, 103167. [CrossRef]
30. Zong, B.; Song, Q.; Min, M.R.; Cheng, W.; Lumezanu, C.; Cho, D.; Chen, H. Deep autoencoding Gaussian mixture model for unsupervised anomaly detection. In *Proceedings of the International Conference on Learning Representations*; Curran Associates Inc.: Red Hook, NY, USA, 2018; pp. 1–19.
31. Bernacki, J.; Kołaczek, G. Anomaly detection in network traffic using selected methods of time series analysis. *Int. J. Comput. Netw. Inf. Secur.* **2015**, *7*, 10–18. [CrossRef]
32. Silverman, B.W. *Density Estimation for Statistics and Data Analysis*, 1st ed.; Routledge: Evanston, IL, USA, 1998.
33. Laptev, N.; Amizadeh, S.; Flint, I. Generic and scalable framework for automated time-series anomaly detection. In Proceedings of the 21th ACM SIGKDD International Conference on Knowledge Discovery and Data Mining, Sydney, Australia, 10–13 August 2015; pp. 1939–1947.
34. Mndela, Y.; Ndou, N.; Nyamugama, A. Irrigation scheduling for small-scale crops based on crop water content patterns derived from UAV multispectral imagery. *Sustainability* **2023**, *15*, 12034. [CrossRef]
35. Levene, H. Robust testes for equality of variances. In *Contributions to Probability and Statistics*; Olkin, I., Ed.; MR0120709; Stanford University Press: Palo Alto, CA, USA, 1960; pp. 278–292.
36. Mulekar, M.S.; Mishra, S.N. Overlap Coefficient of two normal densities: Equal means case. *J. Jpn. Stat. Soc.* **1994**, *24*, 169–180.
37. Kotte, S.; Kumar, P.R.; Injeti, S.K. An efficient approach for optimal multilevel thresholding selection for gray scale images based on improved differential search algorithm. *Ain Shams Eng. J.* **2018**, *9*, 1043–1067. [CrossRef]
38. Domola, M.J.; Thompson, G.J.; Aveling, T.A.S.; Laurie, S.M.; Strydom, H.; Van den Berg, A.A. Sweet potato viruses in South Africa and the effect of viral infection on storage root yield. *Afr. Plant Prot.* **2008**, *14*, 15–23.
39. Huete, A.; Didan, K.; Miura, T.; Rodriguez, E.P.; Gao, X.; Ferreira, L.G. Overview of the radiometric and biophysical performance of the MODIS vegetation indices. *Remote Sens. Environ.* **2002**, *83*, 195–213. [CrossRef]
40. Mulabisana, M.J.; Cloete, M.; Mabasa, K.G.; Laurie, S.M.; Oelofse, D.; Esterhuizen, L.L.; Rey, M.E.C. Surveys in the Gauteng, Limpopo and Mpumalanga provinces of South Africa reveal novel isolates of sweet potato viruses. *S. Afr. J. Bot.* **2018**, *114*, 280–294. [CrossRef]
41. Wright, P.J.; Lewthwaite, S.L.; Triggs, C.M.; Broadhurst, P.G. Laboratory evaluation of sweet potato (*Ipomoea batatas*) resistance to sclerotinia rot. *N. Z. J. Crop Hortic. Sci.* **2003**, *31*, 33–39. [CrossRef]
42. Patel, R.; Fang, F.C. Diagnostic stewardship: Opportunity for a laboratory–infectious diseases partnership. *Clin. Infect. Dis.* **2018**, *67*, 799–801. [CrossRef] [PubMed]
43. Bai, Y.; Zarco-Tejada, P.J.; Peñuelas, J.; McCabe, M.F.; Hawkesford, M.J.; Atzberger, C.; Poblete, T.; Kumar, L.; Reynolds, M.P.; Nie, C.; et al. Hyperspectral Remote Sensing for Monitoring Crop Disease: Applications, challenges, and perspectives. *IEEE Geosci. Remote Sens. Mag.* **2025**, *14*, 96–120. [CrossRef]
44. Sali, A.; Nomqupu, S.; Nyamugama, A.; Ndou, N. Smoke characterization for incipient wildfire detection from Sentinel-2 sensor based on sigmoid activation function and momentum gradient descent optimizer. *Earth Sci. Inform.* **2025**, *18*, 488. [CrossRef]
45. Nomqupu, S.; Sali, A.; Nyamugama, A.; Ndou, N. Integrating Sigmoid Calibration Function into Entropy Thresholding Segmentation for Enhanced Recognition of Potholes Imaged Using a UAV Multispectral Sensor. *Appl. Sci.* **2024**, *14*, 2670. [CrossRef]
46. Gupta, S.; Gupta, A. Handling class overlapping to detect noisy instances in classification. *Knowl. Eng. Rev.* **2018**, *33*, e8. [CrossRef]
47. Xiong, H.; Wu, J.; Liu, L. Classification with class overlapping: A systematic study. In *Proceedings of the International Conference on E-Business Intelligence*; Atlantis Press: Dordrecht, The Netherlands, 2010; pp. 491–497.
48. Devi, D.; Biswas, S.K.; Purkayastha, B. Learning in presence of class imbalance and class overlapping by using one-class SVM and undersampling technique. *Connect. Sci.* **2019**, *31*, 105–142. [CrossRef]

49. Rondeaux, G.; Steven, M.; Baret, F. Optimization of soil-adjusted vegetation indices. *Remote Sens. Environ.* **1996**, *55*, 95–107. [CrossRef]
50. Chandrakar, V.; Pandey, N.; Keshavkant, S. Plant responses to arsenic toxicity: Morphology and physiology. In *Mechanisms of Arsenic Toxicity and Tolerance in Plants*; Hasanuzzaman, M., Nahar, K., Fujita, M., Eds.; Springer: Singapore, 2018; pp. 27–48.
51. Damm, A.; Paul-Limoges, E.; Haghighi, E.; Simmer, C.; Morsdorf, F.; Schneider, F.D.; van der Tol, C.; Migliavacca, M.; Rascher, U. Remote sensing of plant-water relations: An overview and future perspectives. *J. Plant Physiol.* **2018**, *227*, 3–19. [CrossRef] [PubMed]
52. Kranner, I.; Minibayeva, F.V.; Beckett, R.P.; Seal, C.E. What is stress? Concepts, definitions and applications in seed science. *New Phytol.* **2010**, *188*, 655–673. [CrossRef] [PubMed]
53. Jenerowicz, A.; Wierzbicki, D.; Kedzierski, M. Radiometric Correction with Topography Influence of Multispectral Imagery Obtained from Unmanned Aerial Vehicles. *Remote Sens.* **2023**, *15*, 2059. [CrossRef]
54. Ndou, N.; Thamaga, K.H.; Mndela, Y.; Nyamugama, A. Radiometric Compensation for Occluded Crops Imaged Using High-Spatial-Resolution Unmanned Aerial Vehicle System. *Agriculture* **2023**, *13*, 1598.
55. Haralick, R.M.; Shanmugam, K.; Dinstein, I. Textural features for image classification. *IEEE Trans. Syst. Man Cybern.* **1977**, *SMC-3*, 610–621. [CrossRef]

Disclaimer/Publisher's Note: The statements, opinions and data contained in all publications are solely those of the individual author(s) and contributor(s) and not of MDPI and/or the editor(s). MDPI and/or the editor(s) disclaim responsibility for any injury to people or property resulting from any ideas, methods, instructions or products referred to in the content.